Optimized Infrared LED and its use in an all-HgTe Nanocrystal-based active imaging setup

Erwan Bossavit, Junling Qu, Claire Abadie, Corentin Dabard, Tung Dang, Eva Izquierdo, Adrien Khalili, Charlie Gréboval, Audrey Chu, Stefano Pierini, et al.

Optimized Infrared LED and its use in an all-HgTe Nanocrystal-based active imaging setup

Erwan Bossavit[1], Junling Qu[1], Claire Abadie[1], Corentin Dabard[1], Tung Dang[1], Eva Izquierdo[1], Adrien Khalili[1], Charlie Gréboval[1], Audrey Chu[1], Stefano Pierini[1], Mariarosa Cavallo[1], Yoann Prado[1], Victor Parahyba[2], Xiang Zhen Xu[3], Armel Decamps-Mandine[4], Mathieu Silly[5], Sandrine Ithurria[3], Emmanuel Lhuillier[1*]

[1] Sorbonne Université, CNRS, Institut des NanoSciences de Paris, INSP, F-75005 Paris, France.
[2] New Imaging Technologies SA, 1 impasse de la Noisette 91370 Verrières le Buisson, France.
[3] Laboratoire de Physique et d'Etude des Matériaux, ESPCI-Paris, PSL Research University, Sorbonne Université Univ Paris 06, CNRS UMR 8213, 10 rue Vauquelin 75005 Paris, France.
[4] Centre de MicroCaractérisation Raimond Castaing, UAR3623, CNRS, Université de Toulouse, 3 rue Caroline Aigle, 31400 Toulouse, France
[5] Synchrotron-SOLEIL, Saint-Aubin, BP48, F91192 Gif sur Yvette Cedex, France.

Abstract: Nanocrystals have reached a high level of maturity, enabling their integration into optoelectronic devices. The next challenge is the combination of several types of devices into one complex system to achieve better on-chip integration. Here, we focus on an all-HgTe-nanocrystal active imaging setup operating in the short-wave infrared. We first focus on the design of an optimized infrared light emitting diode (LED). We show that a halide technology processing enables an increase of the electroluminescence signal by a factor of 3, while preserving a low turn-on voltage and a high brightness (3 $W.sr^{-1}.m^{-2}$). We then unveil the degradation mechanism of this LED under continuous operation and show a shift from band edge to trap emission. This degradation process can be strongly reduced thanks to the encapsulation and the thermal control of the LED. Lastly, we image the infrared emission of the LED using a focal plane array whose active layer is also made of HgTe nanocrystals, paving the way for all-nanocrystal-based active imaging setups.

Keywords: LED, infrared, nanocrystal, HgTe, active imaging, electronic temperature, focal plane array.

*To whom correspondence should be sent: el@insp.upmc.fr

Introduction

Thanks to a careful control of the size distribution, nanocrystals (NCs) can achieve tunable band edge optical features combined with narrow light emission spectra. These properties have been widely used for applications such as display down-converters, single photon sources[1,2] and bioimaging. As their optical features became more and more mature, the charge conduction within NC arrays has also been tackled, enabling their integration into optoelectronic devices[3] such as light emitting diodes[4–6] (LED), solar cells and infrared (IR) focal plane arrays[7]. Individually some of these devices are now reaching a commercial status. The next challenge is to push further the integration of NCs and to use them as a platform for on-chip applications. The concept is to combine, on the same device, several functionalities (light emission, light detection, gas sensing, temperature sensing, *etc*…) to generate a complex system. A typical application of such a concept is gas sensing: an IR emitter is coupled to a detector which collects the change in light intensity induced by the absorption of the gas molecular vibration. Another example is communication, as recently demonstrated with LiFi like communication obtained[8] by coupling an all-NC-based visible LED to a solar cell. Here, we target active imaging. Active imaging is an infrared imaging at wavelengths below thermal emission where a non-visible source is used to illuminate the scene. Active imaging is used for LIDAR detection or industrial vision (trash sorting, moisture detection…). The goal of this paper is to demonstrate an all-nanocrystal-based active imaging setup operating in the short-wave infrared (SWIR). To do so, we build a bright LED and image its electroluminescence (EL) signal on a camera. In both systems we target to use NCs as the active material.

In this paper, we choose to focus on HgTe NCs[9] as the active material since they present a high maturity on the detection side[10–12], and LEDs based on HgTe NCs have already been reported[13]. NC-based LEDs[14] are one of the most complex devices to design because it requires preserving the material luminescence while enabling charge conduction. Although tremendous efforts have been dedicated to this question in the visible range, far less work has focused on IR wavelengths. PbS[15,16] and Ag_2S NCs[17] have been used to obtain electroluminescence in the near infrared and up to telecom wavelengths. HgTe being a semimetal under bulk form, it enables a unique spectral tunability from 800 nm for strongly confined forms[18], up to the THz range[19,20] for the largest particles. Such broadband tunability has led to the first demonstration of EL above 2 µm[21], which paves the way for mid-IR emission and possible applications such as gas sensing. Even though bright emission (*i.e.,* high radiance) is achieved using HgTe NCs, the external quantum efficiency (EQE) remains below the ones reported for PbS and Ag_2S NCs[16,17] at the same wavelength, raising the need for optimization. To address this issue, we explore alternative surface chemistries to halide-based short thiols. We demonstrate that EQE can be enhanced by a factor of 2-3 by using a two-step procedure combining thiol and iodide as capping agents. We also carefully explore the degradation mechanism at play that is currently limiting the device lifetime. Finally, we show that the EL signal from HgTe NCs can be imaged using a focal plane array whose active layer is made of HgTe NCs. This result paves the way for the design of all-nanocrystal-based active imaging setups in the SWIR.

Results and discussion

To achieve EL from HgTe NCs, we use a structure inspired by solar cells[22]. The structure is made of the stack of ITO/ZnO/ZnO+HgTe mixture/PbS/Au, as initially proposed by Pradhan *et al*[16] for PbS NCs and later applied to HgTe by Qu *et al*[13]. Here ITO and ZnO layers are used as electron injectors, while short thiol capped PbS coupled with the gold electrode serve as hole injectors. To build such a stack ZnO[16], PbS[23] and HgTe[24] are colloidally grown, see TEM pictures in **Figure 1**b-d. ZnO is a wide band gap material and is optically inactive in the infrared. However, both PbS (0.95 µm absorption edge – 1.1 µm peak PL, see **Figure 1**f) and HgTe (1.2 µm absorption edge - PL peak around 1.3 µm, see **Figure 1**g) present a luminescence in the near IR. The band edge of

PbS is chosen wider than that of HgTe so that finally EL signal only results from HgTe as confirmed later.

The band alignment and the role of ZnO in the emitting layer (formation of a bulk heterojunction with HgTe to ensure both hole and electron conductions) have been revealed in our previous work[13]. This is why we focus here on the structural properties of the diode. A side view of the device can be obtained by slicing the device using a focus ion beam and then imaging this slice using transmission electron microscopy, see **Figure 1**a. Though the contrast of the TEM image is already enough to identify the different components of the stack, the device composition is better highlighted using Scanning TEM High-Angle Annular Dark-Field (STEM-HAADF) imaging coupled to energy dispersive X-ray spectroscopy (EDX), see **Figure 1**e. STEM EDX imaging confirms the absence of interdiffusion between the different nanocrystal populations.

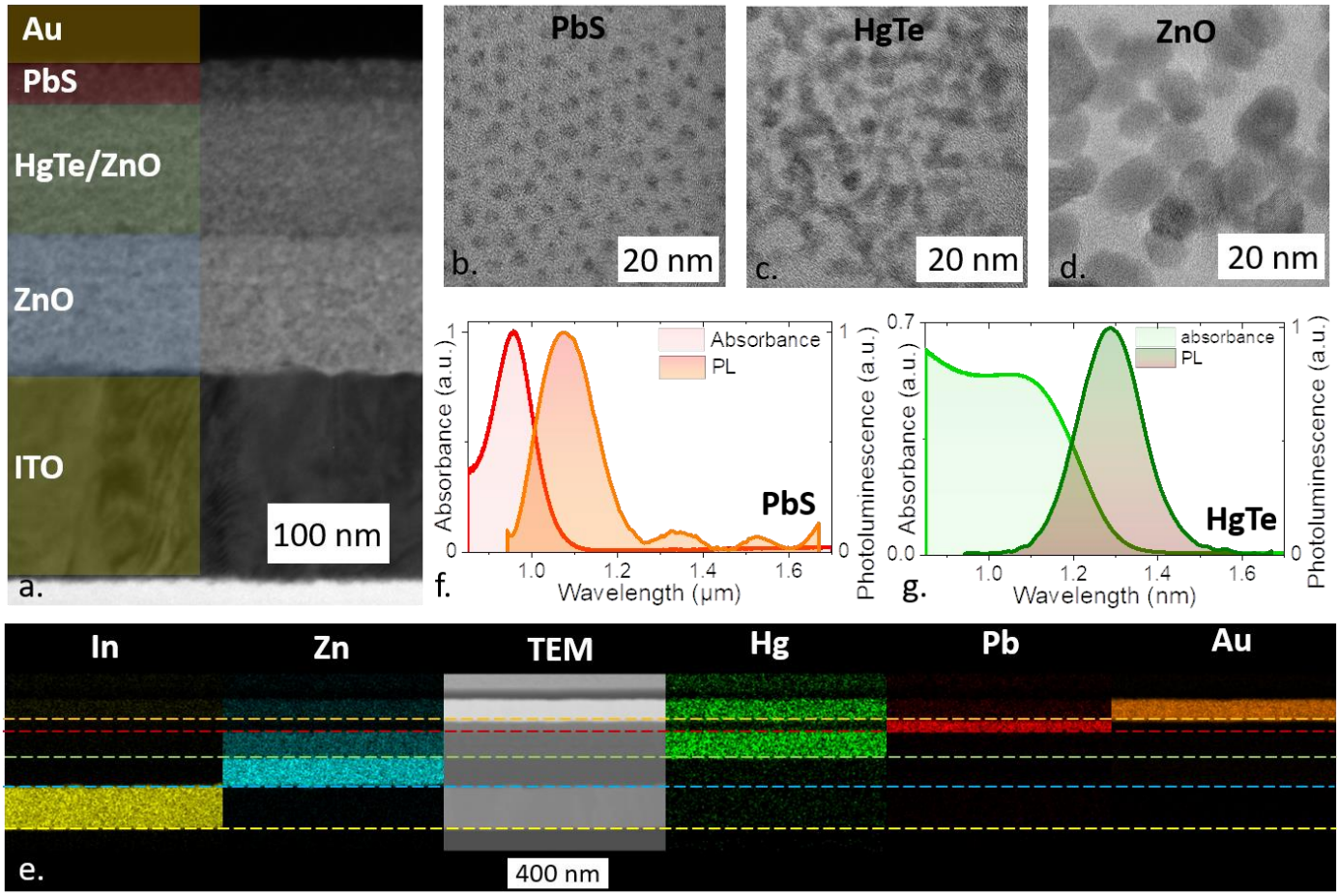

Figure 1 LED stack structure*. a. Side view image of the LED stack taken with a TEM. False colors have been added on the left side to correlate each layer to its content. b-d are respectively TEM images of the PbS, HgTe and ZnO particles used to build the LED stack. e. HAADF STEM side view and EDX mapping for In, Zn, Hg, Pb and Au. f. Absorption and PL of PbS NCs used as a hole injector layer. g. Absorption and PL of HgTe NCs used as an emitting layer. Note that Hg detected in the Au layer is due to overlap from the Hg signal with the Au EDX signal.*

The initial (*i.e.,* in solution) photoluminescence quantum yield (PLQY) of the HgTe NCs has been measured to be around 45%[13]. Yet, the best EQE for this LED stack was calculated/measured? at around 0.6%, suggesting that further optimizations are required. The current procedure to build the LED relies on a ligand exchange of the HgTe/ZnO layer using short thiols (3-mercaptopropionic acid, MPA). The latter is critical to make the film conductive and form a thick emitting layer. However, it also strongly reduces the PLQY, as shown in **Figure 2**a. On the other hand, we observe that the

surface can be healed by treating the NCs with mercury halides. The PLQY can even exceed the value obtained for the pristine film in the case of $HgBr_2$ and HgI_2, see **Figure 2**b. Note that the halide ligand exchange also induces a spectral shift (blue shift for Cl and redshift for Br and I). The redshift can be attributed to a stronger packing between particles as the ligand length is reduced. On the other hand, the blue shift observed for Cl is certainly resulting from a dipole or partial etching of the surface.

Mercury halide solid state ligand exchange alone does not cross link the film and it is not possible to form a thick conductive film while only using these ligands. Therefore, we develop a two-step ligand exchange procedure: we first use MPA to cross link the film and achieve a conductive film and then heal the surface by exposing the film to a mercury halide solution. X-ray photoemission (figure S1) confirms the presence of iodide on the final material. In this case, LED EQE is enhanced compared to the diode only processed with MPA. Using MPA+HgI_2 the EQE now reaches 2.2 % (*i.e.,* x 3 compared to MPA-only device, see **Figure 2**c-d). Though it is still weaker than the values reported with PbS and Ag_2S, this value remains the largest obtained for HgTe-based LEDs, see table S3 for a comparison with state-of-the-art LED.

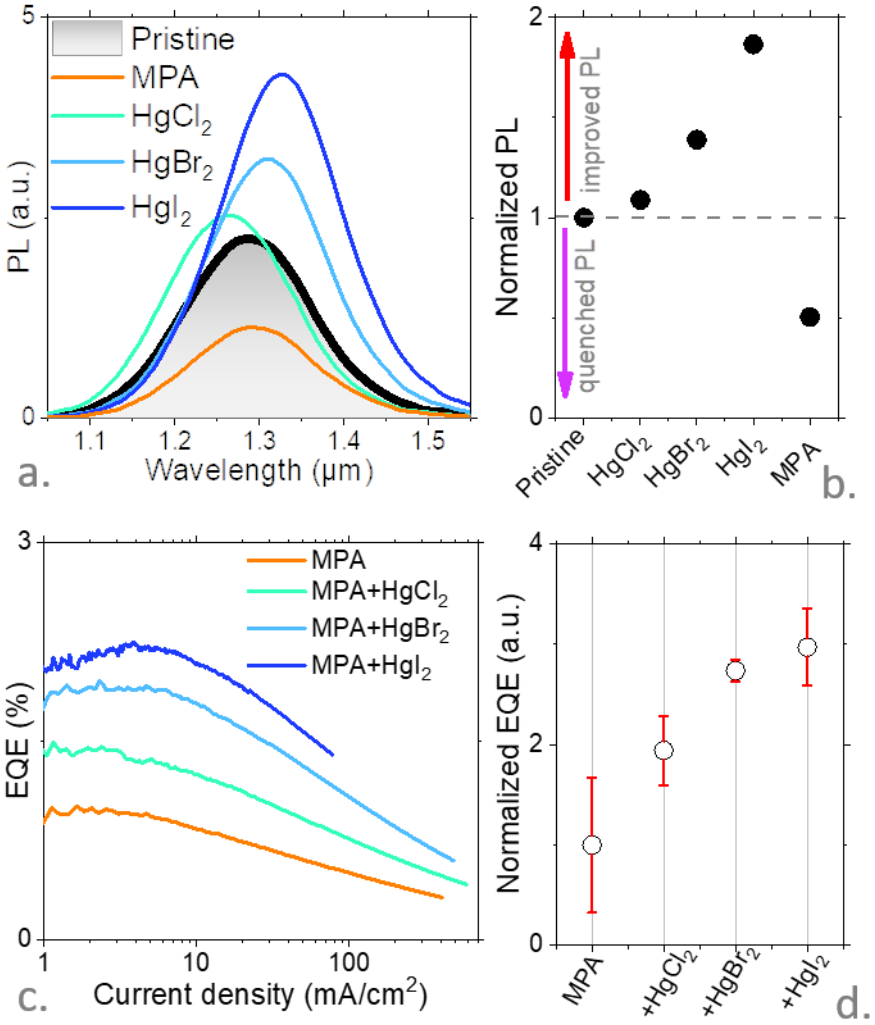

Figure 2 Surface healing using mercury halide and its impact on PL and EL signals. *a. PL of a HgTe thin film processed with MPA or MPA and mercury halide. b. Magnitude of the PL signals, normalized by the value of the pristine film (i.e., HgTe capped with DDT) for HgTe NC thin films processed with various surface chemistries. c. LED external quantum efficiency as a function of the injected current density for LEDs where the emitting layer is processed with various surface chemistries. d. Relative magnitude of the EQE, normalized by the value where HgTe is processed with MPA.*

Since the iodide treatment leads to the highest performance, we then focus the characterization of the device based on this surface chemistry, see **Figure 3**. **Figure 3**a depicts the current and radiance as a function of the applied bias. It reveals a 0.8 V turn-on voltage corresponding to a sub band gap operation. The radiance reaches 3 $W.sr^{-1}.m^{-2}$ under 6 V of bias. The EL spectra are shown in **Figure 3**b and a small blueshift is observed as higher currents are used to drive the LED. Note that no feature from PbS (PL maximum at 1100 nm) is observed in the spectrum of the LED.

According to the Kirchhoff law,[25,26] the spontaneous emission spectra *EL* of the material relates to the absorption *A* by the relation $EL(\lambda) \propto A(\lambda).W(\lambda,T_e)$, where *W* is the Planck's law and T_e the electronic temperature. The Wien approximation leads to $W(\lambda,T_e)=2hc^2\lambda^{-5}\exp[-hc/(\lambda k_B T_e)]$, where *h* and k_B are the Planck and Boltzmann constants and λ is the photon wavelength. As a result, there is a value of T_e, which should make the quantity $EL(\lambda)/W(\lambda,T_e)$ a constant for all operating conditions (*i.e.,* any bias or any driving current). Moreover, we assumed that the electronic temperature close to the turn-on voltage was the same as the lattice temperature (*i.e.,* room temperature). We then renormalized all EL spectra to this spectrum close to the threshold and used the electronic temperature as a fitting parameter to make the $EL(\lambda,V)/W(\lambda,T_e)$ overlap with the EL (λ,V=turn-on voltage)/$W(\lambda,T_e$=290 K), see Figure S2. Thus, we can have an estimation of the electronic temperature directly from the EL spectrum, see **Figure 3**c. The values of T_e that we obtain are much higher that the device temperature revealed from thermal imaging. This expresses the out of equilibrium operation of LED. Interestingly we notice a power law scaling between T_e and J the driving current density with $T_e \propto J^{0.05}$. Such scaling will be useful to later identify conservative operating conditions of LED

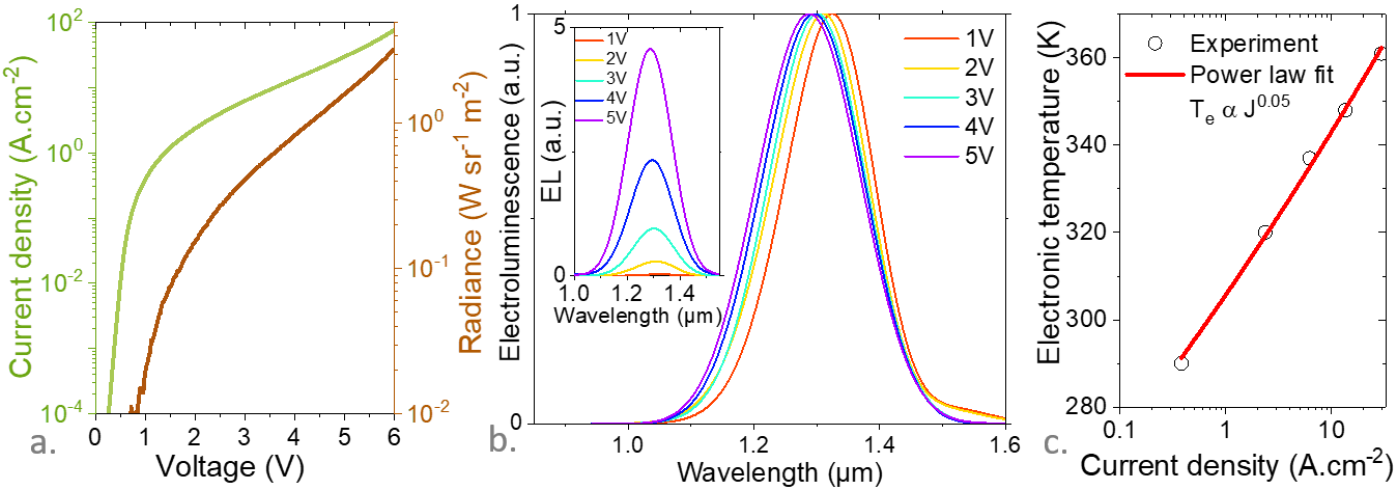

***Figure 3 Performance of the HgI_2 treated LED**. a. Current density and irradiance as a function of the applied bias for the LED where the active layer is processed by a MPA and then by HgI_2. b. Normalized electroluminescence signals for different applied biases, highlighting a clear blue shift as the bias is increased. The inset is the non-normalized data. c. Electronic temperature as a function of the driving current of the LED.*

We then investigate the aging of the diode under operation. As the LED is driven under a constant current, we observe two regimes, see **Figure 4**a. At first, we observe an increase of the emitted power. For an encapsulated LED this regime lasts 50 to 100 h, before the power starts to drop. This change of the output power also comes with a strong redshift of the EL signal, see **Figure 4**. The initial EL peak shifts from 1250 to above 1500 nm after 180 h of continuous operation. The LED is also more resistive (**Figure 4**c) which results in reduced radiance when operated under the same conditions. Such a large spectral shift may be interpreted as an increase in the effective NC radius leading to a reduction of quantum confinement. This effect may typically result from the high

temperature operation of the LED when driven under continuous current. However, this hypothesis is unlikely given the fact that the emitting layer is made of an HgTe/ZnO mixture and thus a given HgTe NC is not necessarily surrounded by another HgTe NC. To clarify this point we have followed the spectrum as a function of time (**Figure 4**d) for a non-encapsulated LED, in which degradation is prompted compared to the encapsulated device. It appears that the EL signal is not continuously shifting, but rather that it includes two components. The amplitude of the band edge component quickly collapses and is replaced by a lower energy one (see inset of **Figure 4**d), which was previously attributed to trap states[27] near the valence band resulting from surface Te excess[24].

At long time scales, the amplitude of this low energy component also collapses, which explains the reduction of the signal observed. Degradation in this diode appears to have a specific mechanism where the desorption of ligands, likely resulting from the heating of the diode under operation, leads to a transfer of the radiative process from band edge to emissive trap states. We also identify strategies to increase the device lifetime. Encapsulation of the device (using epoxy and top sapphire substrate as coating) postpones the time when power decreases by a factor of almost 100, from below 1 h to around 50 h (**Figure 4**e). Furthermore, the addition of a Pelletier stage to extract the heat increases the duration to reach the maximum power beyond 150 h of continuous operation, see **Figure 4**e.

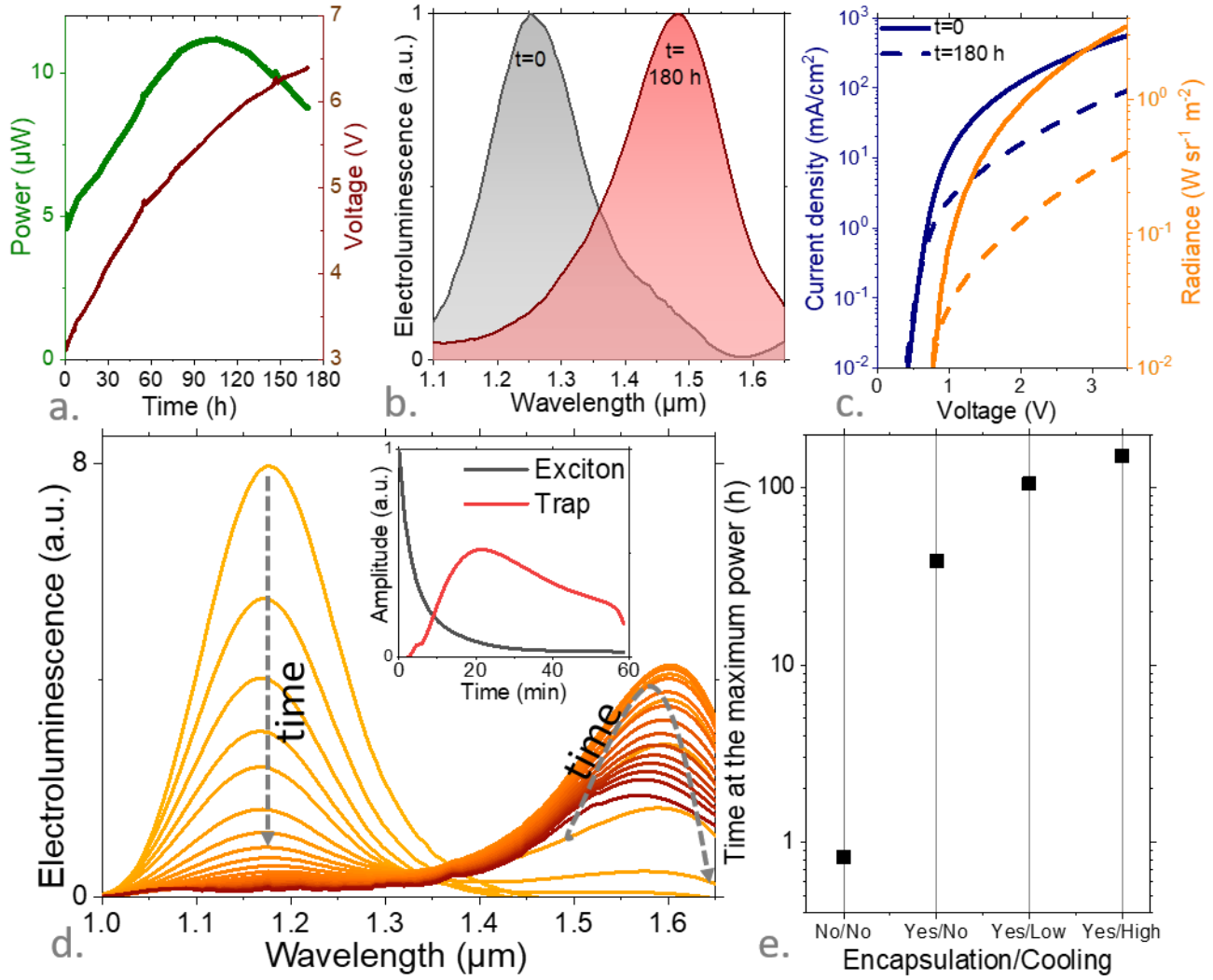

Figure 4 Aging mechanism of the LED*. a. Time dependence of the power and the voltage for a LED driven at a constant current (5.9 mA) corresponding to an initial irradiance of 3 W.sr^{-1}.m^{-2}. b. EL spectra for a LED after fabrication and after 180 h of continuous operation under 5.9 mA. c. Current density and radiance as a function of bias for a LED after fabrication and after 180 h of continuous operation under 5.9 mA. For part a to c the used LED has I$^-$ as surface chemistry, encapsulation and no cooling. d. EL spectra at various times (from light to dark colors corresponds*

from early to long time, the darkest one corresponds to one hour operation) for a LED (without encapsulation) under continuous operation at 5.5 mA. The inset is the magnitude of the high (around 1.15 µm) and low (1.6 µm) energy contributions of the EL spectrum as a function of time. e. Time to reach the maximum for various states of the LED (with and without encapsulation or cooling) for operation at (from left to right) 9, 5.9, 5.0, and 7.5 mA corresponding to the same initial irradiance around ≈3 W.sr^{-1}.m^{-2}.

In the last part of the paper, we designed an all-HgTe-NC-based active imaging setup. In addition to the previously designed LED, we built a focal plane array based on CMOS read out circuit (NIT 1601) functionalized by a thin film of HgTe NCs. Here we choose HgTe NCs with a cut-off wavelength of 2 µm to ensure that we collect all the EL signal from the LED. An image of the setup is given in **Figure 5**a. We then used this setup to image the infrared emission of the LED under operation, see **Figure 5**b-c and video S1 for a movie of it. SWIR images of the setup reveal the emission of light by the LED, while the visible image (Figure S3) remains unchanged.

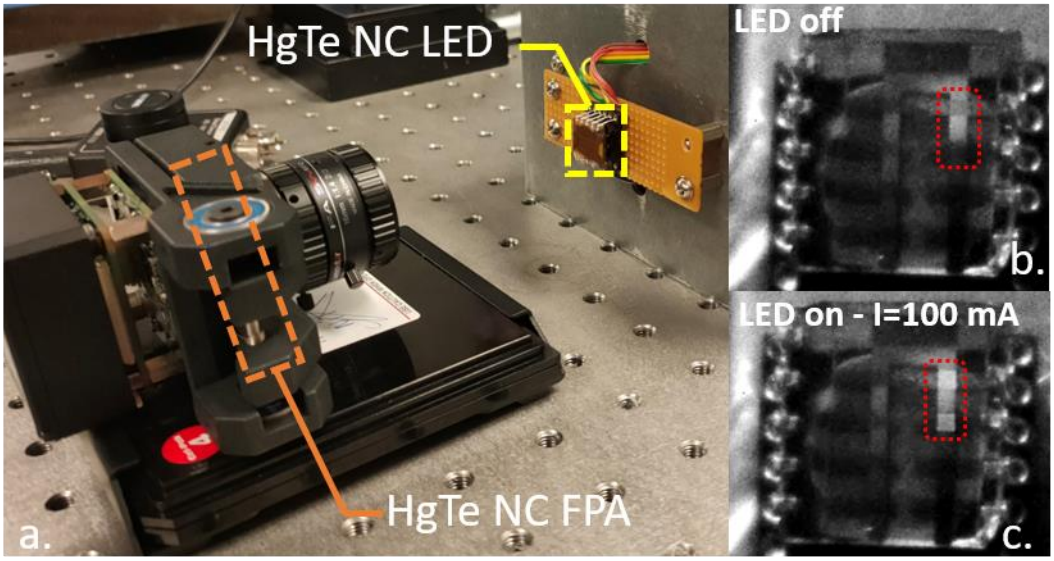

Figure 5 Imaging HgTe IR EL signal using HgTe-NC-based focal plane array. *a. Image of the camera based on HgTe NCs imaging and a HgTe-NC-based LED. b. Image of the off LED. c. Image of the on LED (I=100 mA, two pixels on). The red rectangle is there to locate the two turn-on pixels in parts b and c.*

Conclusion

To summarize, we have designed an HgTe-NC-based LED with shortwave infrared emission. We demonstrate that a halide treatment can cure the surface and enhance the PL efficiency. This process leads to a LED with an EQE up to 2.2%. The structural investigation of the ITO/ZnO/ZnO+HgTe/PbS/Au stack shows no interdiffusion of the different layers. The initial EL signal, corresponding to the band edge of HgTe, shows a sub band gap turn on voltage (0.8 V) and a radiance reaching 3 W.sr^{-1}.m^{-2}. We observe a systematic blue shift when a higher operating bias is applied and we can relate that through Kirchhoff's law to an increase of the electronic temperature above room and even lattice temperature. Interestingly, we determine a scaling law for the electronic temperature as a function of the applied current which can be used later to determine the conservative operation conditions of the LED. We identify two regimes for the aging of the LED. At first, EL emission shifts from band edge to trap emission and then only the EL magnitude drops. We demonstrate that encapsulation and cooling can delay degradation by a factor of 100. Finally, we

succeed in imaging the LED under operation using an HgTe-nanocrystal based focal plane array. This combination of two IR NC-based devices paves the way for a more cost-effective active imaging setup.

Experimental section

Chemicals: Mercury chloride ($HgCl_2$, Strem Chemicals, 99%), mercury bromide ($HgBr_2$, Alfa Aesar), mercury iodide (HgI_2,Touzart & Matignon), tellurium powder (Te, Sigma-Aldrich, 99.99%), octadecene (ODE, Acros Organics, 90%), lead oxide (PbO, Strem Chemicals, 99.999+%-), Zinc acetate dihydrate ($Zn(CH_3COO)_2$, Sigma, 99.999%), oleic acid (OA, Alfa Aesar 90%), hexamethyldisilathiane (TMS_2S, Sigma Aldrich, synthesis grade), hydrochloric acid (HCl, Mieuxa, 25%), potassium Hydroxide (KOH, Sigma 90%), Ammonium iodine (NH_4I, Alfa Aesar, ≥ 99%), 3-mercaptopropionic acid (MPA, Sigma-Aldrich, ≥99.9%), 1,2 ethanedithiol (EDT, Fluka, 98%), trioctylphosphine (TOP, Cytek, 90%), oleylamine (OLA, Acros, 80-90%), dodecanethiol (DDT, Sigma-Aldrich, 98%), chloroform (Carlo Erba), ethanol absolute anhydrous (Carlo Erba, 99.9%), methanol (Carlo Erba, 99.8%), toluene (Carlo Erba, 99.3%), n-octane (SDS, 99%), n-heptane (Merck, >99%), n-hexane (VWR, 99%), N,N-Dimethylformamide (DMF, Sigma Aldrich), Butylamine (Alpha 99%). All chemicals are used as received, except oleylamine which is centrifuged before used. **Mercury and lead compounds are highly toxic. Handle them with special care.**

1 M TOP:Te precursor: 2.54 g of Te powder are mixed in 20 mL of TOP in a three-neck flask. The flask is kept under vacuum at room temperature for 5 min and then the temperature is raised to 100 °C. Furthermore, degassing of flask is conducted for the next 20 min. The atmosphere is switched to nitrogen and the temperature is raised to 275 °C. The solution is stirred until a clear orange coloration is obtained. The flask is cooled down to room temperature and the color switches to yellow. Finally, this solution is transferred to a nitrogen-filled glove box for storage.

HgTe nanocrystal synthesis: The synthesis is taken from Geiregat *et al.*[24] In a 25 mL three-neck flask, 270 mg of $HgCl_2$ (1 mmol), 1.6 mL (6 mmol) of dodecanethiol and 8 mL of oleylamine are degassed under vacuum at 110 °C for 1 h. The atmosphere is switched to N_2 and the temperature is set to 60 °C. When the temperature stabilizes at 60 °C, 1 mL of TOP:Te solution (1 M) is quickly injected, and the growth is allowed for 1 min. The reaction is quenched by injecting 10 mL of toluene. A water bath is used to further cool down the mixture. The reaction mixture is precipitated by methanol and centrifuged at 6000 rpm for 3 minutes. The supernatant is discarded and the pellet is dispersed in 5 mL of toluene before centrifugating again. This time the supernatant is kept and the pellet of colloidally unstable phase is discarded. These washing steps are carried out another two times. The nanocrystals are precipitated one last time in methanol then vacuum dried. Finally they are stored in toluene at a concentration of 30 $mg.mL^{-1}$. The solution is filtered with a 0.22 µm PTFE filter before use.

ZnO nanocrystal synthesis: The synthesis is taken from Pradhan *et al.*[16] Zinc acetate dihydrate (0.98 g) is dissolved in 42 ml of methanol under vigorous stirring and the temperature of the solution is set at 60 °C. In a separate vial, 0.49 g of KOH (90%) are dissolved in 22 ml of methanol. The KOH solution is added dropwise to the zinc acetate solution over the course of 4 min at a constant temperature of 60 °C with stirring. The reaction mixture is kept under the same conditions for the next 2.5 h. At the end of the reaction, the heating mantle is removed, and the solution naturally cools down to room temperature. The reaction mixture is separated in 2 flasks and centrifuged at 6000

rpm for 3 min. After trashing the supernatant, equal amounts of methanol are added to mix with the pellet, and another centrifugation is conducted. After three rounds of purification, the NCs are dispersed in a mixed solvent with 2% butylamine in chloroform. The concentration of ZnO nanoparticles is set at 30 $mg.mL^{-1}$, and they are filtered through 0.22 µm PTFE filter before use.

PbS nanocrystal synthesis: The procedure is inspired by Hines *et al*.[23] 0.9 g of PbO are introduced in a 100 mL three neck flask with 3 g of OA and 47 g of ODE. The flask is degassed under vacuum at 120 °C for 2 hours. Meanwhile, in an air-free glove box, a mixture of 420 µL of TMS_2S and 10 mL of ODE is prepared in a 20 mL vial, then introduced into a 20 mL syringe. The atmosphere of the flask is switched to Ar and the temperature is set equal to 90 °C. The TMS_2S solution is quickly injected and the solution turns dark while the temperature drops to 80 °C. After 8 min at 80 °C, the reaction is stopped by removing the heating mantle and promptly cooling the flask by adding a mixture of heptane and OA. The nanoparticles are then precipitated by the addition of ethanol. The formed pellet is redispersed in toluene. A second step of cleaning is repeated. Finally, the pellet is redispersed in toluene with a 50 $mg.mL^{-1}$ concentration. The solution is centrifuged to remove any colloidally unstable material. Finally, the solution is filtered on a 0.22 µm PTFE filter. The absorption edge appears around 960 nm (1.3 eV), see **Figure 1**. The material is also photoluminescent and the maximum of the emission is around 1100 nm.

Electronic microscopy image on device: The TEM slice was prepared using a FEI Helios NanoLab600i dual beam SEM FIB fitted with an EasyLift micromanipulator for in situ lift-out. The ion column was operated at 30 kV for all the steps, except for final cleaning of the sample, for which tensions of 5 kV and 2 kV were used. The beam currents varied between 47 nA and 15 pA. The electron beam was used to deposit a 20 nm thick C layer over an area of 20 µm x 2 µm. The ion beam was then used to deposit a 3 µm thick layer Pt over the same area. The slice was partially cut out and a Pt needle was fixed. The sample was lifted out in situ and then attached to a copper support grid. Thinning of the sample could then be processed using a gradual cross-section cleaning milling pattern, with a final milling beam current of 80 pA. Finally, the 5 kV and 2 kV cleaning steps were carried out on each side. The TEM images were performed with a JEOL 2100F TEM. The gun is a Schottky emitter used with a high voltage of 200kV. The slice was observed with a Gatan Ultrascan Camera in TEM mode. The EDS spectrum and mapping used a Bruker SDD. All the STEM images were done using HAADF STEM detector.

TEM of NCs: A drop of a diluted nanocrystal solution is drop-casted on a copper grid covered with an amorphous carbon film. The grid is degassed overnight under secondary vacuum. Imaging is conducted using a JEOL 2010 transmission electron microscope operated at 200 kV.

UV-Vis spectrum of nanocrystal solution is recorded using a JASCO V-730 spectrometer. When a combination of UV and NIR measurement is required, we use a Shimadzu 3600 UV-Vis-NIR.

Infrared spectroscopy is conducted using a Fisher IS50 Fourier transform Infrared spectrometer. To measure the NC absorption, we use the spectrometer in ATR configuration. A drop of NC solution is dried onto the diamond cell. The source is a white light, the beam splitter is made of CaF_2 and the detector is a DTGS ATR. Spectra are typically acquired between 12 000 cm^{-1} and 2000 cm^{-1} with a 4 cm^{-1} resolution while averaging over 32 spectra.

ITO patterning: We start with commercial glass/ITO substrates of 30x30 mm² with a low sheet resistance (7 Ω/□). Substrates are cut into 15x15 mm² pieces and cleaned by sonication in an acetone bath during 5 min. The cleaning procedure is followed by rinsing the substrates with acetone and iso-propanol, then dried with a dry N_2 flow. Then, 5-min plasma cleaning is conducted on the surface of ITO. AZ 5214E photoresist is spin-coated for 30 s, then baked at 110 °C for 90 s. A standard photolithography process is performed using a mask aligner and exposing the substrates to UV light for 20 s through a lithography mask (1 mm width). Photoresist is developed using AZ 726 developer for 20 s and the sample is immediately rinsed with deionized water. After that, exposed ITO surface is completely etched out with 25% HCl (in water) for 10 min at 40 °C, and the substrates are immediately dipped into deionized water. Then, we conduct lift-off process in an acetone bath. The patterned ITO substrates are cleaned with acetone and isopropanol before use.

***n* -type ZnO layer deposition**: On a patterned ITO substrate, a layer of ZnO is spin coated at a speed of 4000 rpm for 30 s. The film is subsequently annealed at 250 °C on a heating plate for 5 min. The above steps are repeated once more to obtain a ZnO film of 100 nm.

HgTe-ZnO emitting layer preparation: The previously prepared HgTe and ZnO solutions are mixed in a new vial with a one-to-one volume ratio. The vial is agitated and sonicated to ensure homogeneous mixing. 70 µL of the mixed solution are deposited on the ZnO-coated substrate and spun at 4000 rpm for 15 s using a spin coater. For solid state ligand exchange, several drops of a 4 mM MPA solution in methanol are casted on the film and kept there for 15 s. The MPA solution is dried by spinning at 4000 rpm. The excess ligands are rinsed off twice with methanol by drop casting and spinning. A second ligand exchange is carried out using a 5 mM HgX_2 (X=Cl, Br, I) solution in methanol and following the same deposition and washing steps as with MPA. For each device, 3 layers (≈120 nm) are deposited this way.

PbS hole injector: To build a hole injection layer, PbS nanocrystals absorbing at 960 nm are used. Inside a glovebox, a PbS solution (30 $mg.mL^{-1}$ in toluene) is spin coated at 2500 rpm on top of MPA-capped HgTe/ZnO emitting layers. EDT in acetonitrile (0.03%) is used for the ligand exchange. The EDT drops are kept on the film for 1 min before drying, and rinsing twice with acetonitrile. Three layers of EDT-capped PbS are deposited successively to achieve an overall thickness of 50 nm.

Top contact: After the deposition of PbS nanocrystal layers, the sample is put into a thermal evaporator. 80 nm of Au is deposited in a vacuum below $5x10^{-6}$ mbar.

Encapsulation procedure: In order to isolate the devices from ambient air, they are encapsulated using sapphire. In a glove box filled with N_2 atmosphere, one or two drops of UV curable epoxy (encapsulation epoxy E132 from Ossila) are put on top of all the previously deposited layers. A sapphire substrate is pressed on the device with tweezers so that the epoxy can spread homogeneously between the sapphire and the device. The epoxy is then cured under 365 nm UV light from a UV lamp for 30 minutes.

Electroluminescence: Electroluminescence spectra are collected by a Flame NIR Spectrometer equipped with an InGaAS detector from Ocean optics while passing a constant current with a Keithley 2400. Devices both with and without encapsulation are tested and stored in air atmosphere.

EQE and radiance measurements: Several voltage sweeps (typically between 0 V and 5 V with 20 mV steps) are performed on the individual pixels. During the measurement, current-voltage characteristics are collected with a Keithley K2400 source meter unit while power characteristics are collected using a PM100A power meter coupled with the S122C Ge detector from Thorlabs. Considering the Lambertian emission of LED, the flux leaving the device can be directly described as $F_{ext} = \int_0^{\pi/2} 2\pi L_0 \, cos\theta \, sin\theta \, d\theta = \pi L_0$, with L_0 the flux per solid angle of light leaving the device in the forward direction. Since the solid angle from the photodetector to the light source is $\Omega = \frac{S_1}{l^2}$ with S_1 the area of the detector and l the distance between the light source and detector, then $L_0 = \frac{P_{det}}{\Omega} = \frac{P_{\mathrm{det}} l^2}{s_1}$ and $F_{ext} = \frac{\pi P_{\mathrm{det}} l^2}{s_1}$. The number of photons emitted per second to the forward direction can then be calculated by $N_P = \frac{F_{ext}}{h\nu} = \frac{\pi P_{\mathrm{det}} l^2 \lambda}{s_1 hc}$, with λ the wavelength of electroluminescence, h the Plank's constant and c the speed of light. The number of electrons injected per second can be obtained by $N_e = \frac{I}{e}$, with I the current flow of the device. Thus, the EQE can be calculated as $E = \frac{N_p}{N_e} = \frac{\pi P_{\mathrm{det}} l^2 \lambda e}{s_1 hcI}$. The radiance of the device is $R = \frac{F_{ext}}{\pi s_2} = \frac{\pi P_{\mathrm{det}} l^2}{\pi s_1 s_2}$, with S_2 the area of the pixel.

Lifetime measurements: Individual pixels are driven at a constant current for the duration of the experiment using a Keithley 2400. Current is set so that the initial radiance is $R_0 \approx 3$ W.sr^{-1}.m^{-2}. Either current-voltage-power characteristics or electroluminescence spectra are collected as described in the corresponding section at regular time intervals.

ASSOCIATED CONTENT

Supporting Information include 1. X-ray photoemission, 2. Determination of the electronic temperature, 3. Comparison with state-of-the-art NCs based SWIR LED, 4. Infrared imaging of the operating LED using HgTe NCs. Video S1 shows a video of the blinking LED.

COMPETING INTEREST

The authors declare no competing financial interest.

ACKNOWLEDEGMENTS

The project is supported by ERC starting grant blackQD (grant n° 756225) and Ne2Dem (grant n° 853049). We acknowledge the use of clean-room facilities from the "Centrale de Proximité Paris-Centre". This work has been supported by the Region Ile-de-France in the framework of DIM Nano-K (grant dopQD). This work was supported by French state funds managed by the ANR within the Investissements d'Avenir programme under reference ANR-11-IDEX-0004-02, and more specifically within the framework of the Cluster of Excellence MATISSE and also by the grant IPER-Nano2, Copin (ANR-19-CE24-0022), Frontal (ANR-19-CE09-0017), Graskop (ANR-19-CE09-0026), NITQuantum (ANR-20-ASTR-0008-01), Bright (ANR-21-CE24-0012-02) and MixDferro (ANR-21-CE09-0029). JQ thanks Chinese Scholarship Council for PhD funding while AC thanks Agence innovation defense.

REFERENCES

[1] S. Pierini, M. D'Amato, M. Goyal, Q. Glorieux, E. Giacobino, E. Lhuillier, C. Couteau, A. Bramati, *ACS Photonics* **2020**, *7*, 2265.
[2] R. E. Correa, E. A. Dauler, S. H. Pan, D. Rosenerg, A. J. Kerman, R. J. Molnar, X. Hu, F. Marsili, V. Anant, K. K. Berggren, M. G. Bawendi, *Nano Lett* **2012**, *12*, 2953.
[3] J. M. Pietryga, Y.-S. Park, J. Lim, A. F. Fidler, W. K. Bae, S. Brovelli, V. I. Klimov, *Chem. Rev* **2016**, *116*, 10513.
[4] Y. Shirasaki, G. J. Supran, M. G. Bawendi, V. Bulović, *Nat. Photonics* **2013**, *7*, 13.
[5] X. Dai, Z. Zhang, Y. Jin, Y. Niu, H. Cao, X. Liang, L. Chen, J. Wang, X. Peng, *Nature* **2014**, *515*, 96.
[6] X. Dai, Y. Deng, X. Peng, Y. Jin, *Adv. Mater* **2017**, *29*, 1607022.
[7] A. Chu, B. Martinez, S. Ferré, V. Noguier, C. Grébova, C. Livache, J. Qu, Y. Prado, N. Casaretto, N. Goubet, H. Cruguel, L. Dudy, M. G. Silly, G. Vincent, E. Lhuillier, *ACS Appl. Mater. Interfaces* **2019**, *11*, 33116.
[8] J. Qu, P. Rastogi, C. Gréboval, C. Livache, M. Dufour, A. Chu, S.-S. Chee, J. Ramade, X. Z. Xu, S. Ithurria, E. Lhuillier, *ACS Appl Mater Interfaces* **2020**, *12*, 22058.
[9] C. Gréboval, A. Chu, N. Goubet, C. Livache, S. Ithurria, E. Lhuillier, *Chem. Rev* **2021**, *121*, 3627.
[10] A. Chu, C. Gréboval, Y. Prado, H. Majjad, C. Delerue, J.-F. Dayen, G. Vincent, E. Lhuillier, *Nat. Commun* **2021**, *12*, 1794.
[11] M. Böberl, M. V. Kovalenko, S. Gamerith, E. J. List, W. Heiss, *Adv. Mater* **2007**, *19*, 3574.
[12] Y. Dong, M. Chen, W. K. Yiu, Q. Zhu, G. Zhou, S. V. Kershaw, N. Ke, C. P. Wong, A. L. Rogach, N. Zhao, *Adv. Sci* **2020**, *7*, 2000068.
[13] J. Qu, P. Rastogi, C. Gréboval, D. Lagarde, A. Chu, C. Dabard, A. Khalili, H. Cruguel, C. Robert, X. Z. Xu, S. Ithurria, M. G. Silly, S. Ferré, X. Marie, E. Lhuillier, *Nano Lett.* **2020**, *20*, 6185.
[14] V. Wood, V. Bulović, *Nano Rev* **2010**, *1*, 5202.
[15] N. Tessler, V. Medvedev, M. Kazes, S. Kan, U. Banin, *Science* **2002**, *295*, 1506.
[16] S. Pradhan, F. Di Stasio, Y. Bi, S. Gupta, S. Christodoulou, A. Stavrinadis, G. Konstantatos, *Nature Nanotech* **2019**, *14*, 72.
[17] M. Vasilopoulou, H. P. Kim, B. S. Kim, M. Papadakis, A. E. Ximim Gavim, A. G. Macedo, W. Jose da Silva, F. K. Schneider, M. A. Mat Teridi, A. G. Coutsolelos, A. R. bin Mohd Yusoff, *Nat. Photonics* **2020**, *14*, 50.
[18] E. Izquierdo, A. Robin, S. Keuleyan, N. Lequeux, E. Lhuillier, S. Ithurria, *J. Am. Chem. Soc.* **2016**, *138*, 10496.
[19] N. Goubet, A. Jagtap, C. Livache, B. Martinez, H. Portalès, X. Z. Xu, R. P. Lobo, B. Dubertret, E. Lhuillier, *J. Am. Chem. Soc* **2018**, *140*, 5033.
[20] T. Apretna, S. Massabeau, C. Gréboval, N. Goubet, J. Tignon, S. Dhillon, F. Carosella, R. Ferreira, E. Lhuillier, J. Mangeney, *Nanophotonics* **2021***,* 10, 2753.
[21] J. Qu, M. Weis, E. Izquierdo, S. G. Mizrahi, A. Chu, C. Dabard, C. Gréboval, E. Bossavit, Y. Prado, E. Péronne, S. Ithurria, G. Patriarche, M. G. Silly, G. Vincent, D. Boschetto, E. Lhuillier, *Nat. Photonics* **2021,** in press.
[22] C.-H. M. Chuang, P. R. Brown, V. Bulović, M. G. Bawendi, *Nat. Mater* **2014**, *13*, 796.
[23] M. A. Hines, G. D. Scholes, *Adv. Mater* **2003**, *15*, 1844.
[24] P. Geiregat, A. J. Houtepen, L. K. Sagar, I. Infante, F. Zapata, V. Grigel, G. Allan, C. Delerue, D. Van Thourhout, Z. Hens, *Nat. Mater* **2018**, *17*, 35.
[25] J.-J. Greffet, P. Bouchon, G. Brucoli, F. Marquier, *Phys. Rev. X* **2018**, *8*, 021008.
[26] A. Caillas, S. Suffit, P. Filloux, E. Lhuillier, A. Degiron, *J. Phys. Chem. Lett.* **2021**, *12*, 5123.
[27] S. M. Tenney, V. Vilchez, M. L. Sonnleitner, C. Huang, H. C. Friedman, A. J. Shin, T. L. Atallah, A. P. Deshmukh, S. Ithurria, J. R. Caram, *J. Phys. Chem. Lett.* **2020**, *11*, 3473.